Article

Pectoral Fin-Assisted Braking and Agile Turning: A Biomimetic Approach to Improve Underwater Robot Maneuverability

Qu He [1,2,†], Yunpeng Zhu [1,2,†], Weikun Li [2,3,4,*], Weicheng Cui [2,3,4] and Dixia Fan [2,3,4,*]

1. Zhejiang University-Westlake University Joint Training, Zhejiang University, Hangzhou 310027, China; hequ@westlake.edu.cn (Q.H.); zhuyunpeng@westlake.edu.cn (Y.Z.)
2. Key Laboratory of Coastal Environment and Resources of Zhejiang Province, School of Engineering, Westlake University, Hangzhou 310030, China; cuiweicheng@westlake.edu.cn
3. Institute of Advanced Technology, Westlake Institute for Advanced Study, Hangzhou 310024, China
4. Research Center for Industries of the Future, Westlake University, Hangzhou 310030, China
* Correspondence: liweikun@westlake.edu.cn (W.L.); fandixia@westlake.edu.cn (D.F.)
† These authors contributed equally to this work and are considered co-first authors.

Abstract

The integration of biomimetic pectoral fins into robotic fish presents a promising approach to enhancing maneuverability, stability, and braking efficiency in underwater robotics. This study investigates a 1-DOF (degree of freedom) pectoral fin mechanism integrated into the SpineWave robotic fish. Through force measurements and particle image velocimetry (PIV), we optimized control parameters to improve braking and turning performances. The results show a 50% reduction in stopping distance, significantly enhancing agility and control. The fin-assisted braking and turning modes enable precise movements, making this approach valuable for autonomous underwater vehicles. This research lays the groundwork for adaptive fin designs and real-time control strategies, with applications in underwater exploration, environmental monitoring, and search-and-rescue operations.

Keywords: biomimetics; robotic fish; pectoral fins; underwater robotics; maneuverability; hydrodynamics; bioinspired design; autonomous underwater vehicle

1. Introduction

Fish exhibit remarkable agility and control in their aquatic environments [1], much of which is attributed to their sophisticated use of the pectoral fins [2,3]. In BCF (body caudal/fin) fish, these fins work alongside the caudal fins and serve multiple functions, including propulsion, maneuvering, stabilization, and braking, allowing fish to navigate complex underwater landscapes with precision [4]. The biomechanical and hydrodynamic principles behind pectoral fins have been refined through millions of years of evolution [5–7], offering a rich source of inspiration for innovative robotic designs [8–10].

Understanding the role of the pectoral fins in the locomotion of fish requires examining their anatomical structure and underlying fluid dynamics [11,12]. The pectoral fins are flexible and allow for a range of movements that contribute to the fish's ability to generate thrust, adjust the swimming direction, and maintain stability. By altering the angle, shape, and motion patterns of these fins, fish can execute rapid turns, hover in place, brake over a short distance, and even swim backwards [13]. This versatility is particularly evident in species such as bluegill sunfish and yellow boxfish, which demonstrate exceptional control over their pectoral fin movements to perform intricate maneuvers [1,14,15].

The integration of mechanisms inspired by the pectoral fin into robotic systems has significant potential to advance the field of biomimetic robotics. Current robotic designs often face challenges in replicating the fluid and adaptive movements observed in nature [16–18]. By mimicking the shape and control strategies of the fish pectoral fins, we can develop robots capable of navigating through water with increased efficiency and agility. Such advances could have profound applications in underwater exploration, environmental monitoring, and even search and rescue operations [19–21].

Having established the theoretical foundation for the functionality of the pectoral fin and its potential for biomimetic applications, we now present our research on the SpineWave robotic fish platform. This study addresses three key research questions: (1) How can we effectively translate the complex biomechanics of fish pectoral fins into a simplified yet functional robotic mechanism? (2) What are the quantitative relationships between fin design parameters (angle, deployment speed, actuation pattern) and hydrodynamic performance? (3) How do these optimized parameters translate to real-world performance improvements in a complete robotic system?

To answer these questions, we developed a single-degree-of-freedom pectoral fin mechanism with a four-bar parallelogram linkage system that optimizes fin positioning while maintaining balanced weight distribution. We conducted systematic experiments using a six-axis force sensor to measure lift and drag forces under controlled flow conditions and employed particle image velocimetry (PIV) to analyze the resulting flow patterns. Finally, we implemented the optimized control parameters on the SpineWave platform and quantified performance improvements in braking efficiency and maneuverability. This comprehensive approach bridges the gap between biological inspiration and engineering implementation, advancing the field of biomimetic underwater robotics with practical, data-driven design principles.

2. Materials and Methods

2.1. Pectoral Fin Design

2.1.1. Aim and Background

With the design concept of the pectoral fin established, the next crucial step is to evaluate its effectiveness in real-world conditions. Therefore, we set up an experimental environment that closely replicates the operational conditions that the robotic fish will encounter. In the following, we describe the experimental setup used to test the fin performance under controlled conditions. The pectoral fins of real fish exhibit a high degree of freedom (DOF), allowing for complex and versatile movements essential for efficient swimming, maneuverability, and speed control [12]. Replicating this sophisticated natural mechanism in robotic systems poses significant challenges due to hardware constraints, particularly in terms of the size, weight, and complexity of actuation mechanisms [18,22].

Servos are a popular choice in robotics for actuation due to their precision, reliability, and ease of control [16,23,24]. However, the use of servos in a robotic pectoral fin design inherently limits the degrees of freedom that can be achieved. Specifically, the size, energy, and weight constraints of the robotic fish restrict the feasible number of servos, often limiting the pectoral fin on smaller robots to a single degree of freedom (1DOF) [25,26].

Biologically, many fish brake by a simple abduction/adduction of the pectoral fins, rotating them forward in a single plane to generate drag, while sharp turns arise from an asymmetric one-axis rotation of the outside fin [12]. Even in rapid burst-braking, trout fins pivot about their base as the principal axis, with finer deformations playing a secondary role [27]. These studies show that a single-hinge motion captures the dominant force component in both braking and turning, justifying our 1DOF fin approach.

2.1.2. Design and Construction of the Servo Pectoral Fin Mechanism

Despite the limitation of a 1DOF system, we maximize the functionality of the robotic pectoral fin by aligning the servo's output shaft with the Z axis (vertical). This setup allows the fin to act as a speed brake for rapid stops and improves maneuverability in the X–Y plane, enabling sharp and agile turns similar to those of real fish. To maintain balance and reduce rotational inertia, the heavy servo motors are positioned near the center of gravity, though this places the pectoral fins in a less-than-ideal position. In real fish, the pectoral fins are located at the front, which increases the distance between the thrust-producing fins and the center of mass, improving the turning momentum.

To resolve this, we designed a four-bar parallelogram linkage system that repositions the fins to a more advantageous location while keeping the servo motors near the center of gravity. This system offers optimal fin positioning for enhanced maneuverability while maintaining a balanced and efficient placement of servomotors. The linkage is constructed from 3D-printed PLA (density < 1.25 g/cm^3, Bambulab, Shenzhen, China), whose net buoyancy in water is nearly neutral. By mounting the servomotor at the vehicle's center of mass, and extending the parallelogram linkage forward, we can place the fin up to 20 cm ahead of the motor's center of gravity without shifting the overall center of mass in the submerged robot. This arrangement preserves dynamic stability regardless of fin deployment angle since the heavy motor stays fixed at the geometric center of gravity. As shown in Figure 1, the parallelogram linkage ensures that the output angle (θ_2) corresponds to the servo shaft angle (θ_1).

2.2. Experimental Setup

To evaluate the performance of the pectoral fin mechanism, we developed a comprehensive experimental setup that precisely replicates the hydrodynamic conditions encountered by the robotic fish. The experimental apparatus (Figure 2A) consisted of the following:

- Water circulation tank: A recirculating water tank with flow velocity control.
- Fin mechanism: A stripped down version of the biomimetic pectoral fin mechanism.
- Control system: An ESP32 microcontroller (Adafruit, NY, USA) running Circuit-Python v9.2.8, programmed with the same control algorithms used in the SpineWave robot to ensure consistent behavior.
- Force measurement: An ATI (NC, USA) Gamma US-15-50 six-axis force/torque sensor connected to the fin mechanism via a custom 3D-printed adapter.
- Data acquisition: National Instruments (TX, USA) DAQ for force data collection.
- Flow visualization: A particle image velocimetry (PIV) system consisting of a continuous laser sheet and a high-speed camera for selected experiments.
  - Illumination: 532 nm continuous laser (SM-SEMI-532nm-10W) generating a 2 mm thick horizontal light sheet
  - Tracers: 10-μm hollow glass spheres (Dantec) with specific density 1.1 g/cm³ for flow seeding
  - Imaging: High-speed CCD camera (Photron, 1280 × 1024 pixels) sampling at 105 fps beneath the channel floor
  - Processing: Cross-correlation algorithm with multi-pass scheme and 2 × 3 Gaussian sub-pixel fitting
  - Parameters: 25 × 25 pixel interrogation windows (50% overlap) yielding velocity vectors at 3.75 × 3.75 mm² spatial resolution
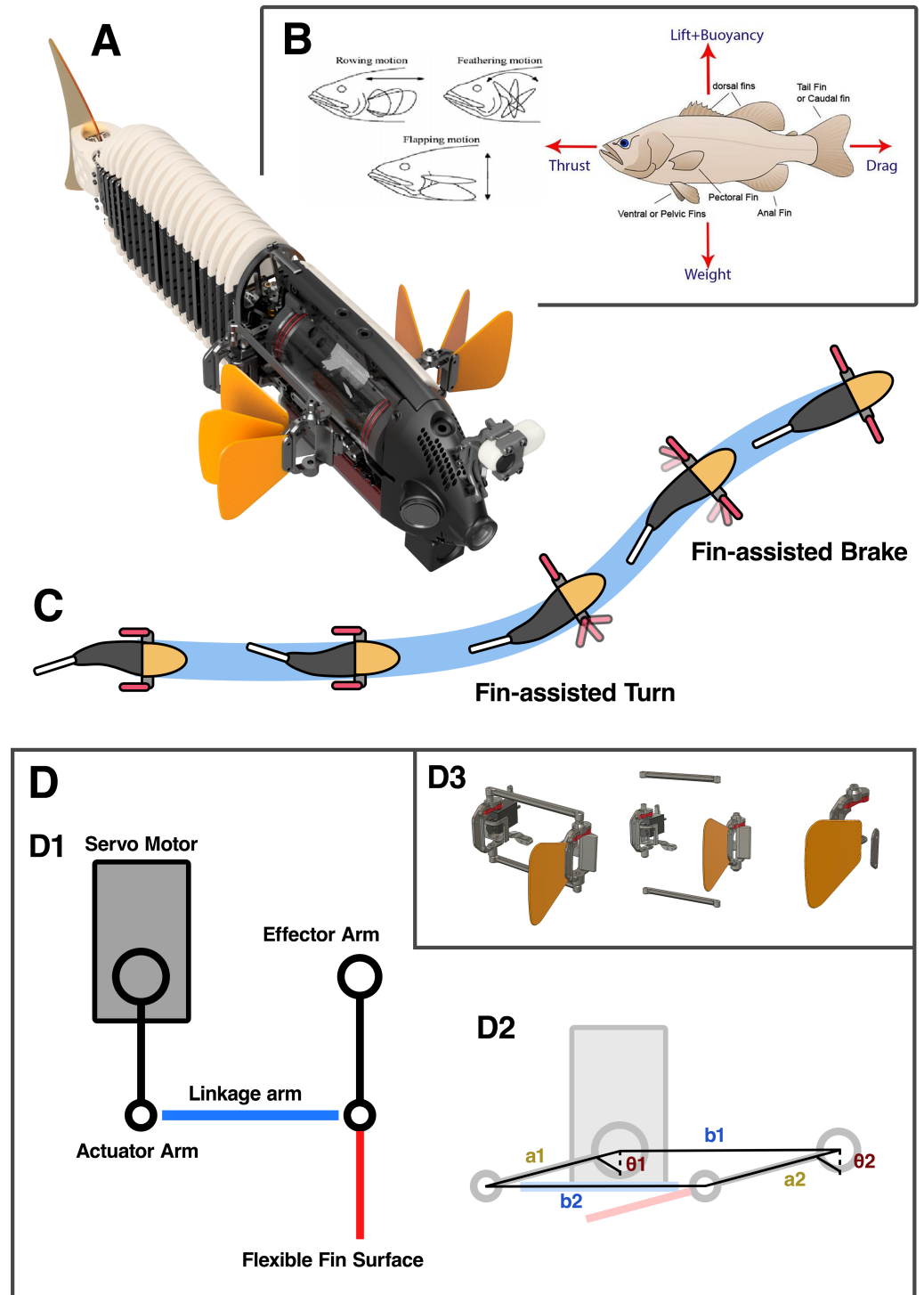
Figure 1. Design of the biomimetic SpineWave robot (**A**), inspired by fish biology, particularly the integration of pectoral fins for enhanced maneuverability and control (**B**). Panel (**C**) illustrates the swimming patterns enabled by the pectoral fin design, including the fin-assisted braking and turning mechanisms. Panel (**D**) provides a detailed view of the pectoral fin actuation system, which incorporates a four-bar parallelogram linkage to ensure optimal fin positioning. Individual components of the actuation mechanism are shown in (**D1**), with (**D2**) depicting the kinematics of the four-bar linkage. (**D3**) offers an exploded view of the fin assembly.

The experimental protocol involved precise control of the fin angle and motion patterns via serial commands from the computer to the ESP32. Each command specified the actuation parameters (angle, frequency, amplitude, and duration) for the specific test condition. Data collection was synchronized with command execution, with force measurements recorded continuously. For each experimental condition, we performed a minimum of five repetitions to ensure statistical reliability.

We used a laboratory-scale hydraulic channel to provide precise flow speed and turbulence control, allowing us to isolate individual variables and collect reproducible, high-resolution force and PIV data. Since field tests introduce many uncontrollable factors (currents, waves, debris) that would obscure fundamental hydrodynamic mechanisms, our data collection is conducted in a controlled lab environment, then transferred to a robotic fish to be tested in open water.
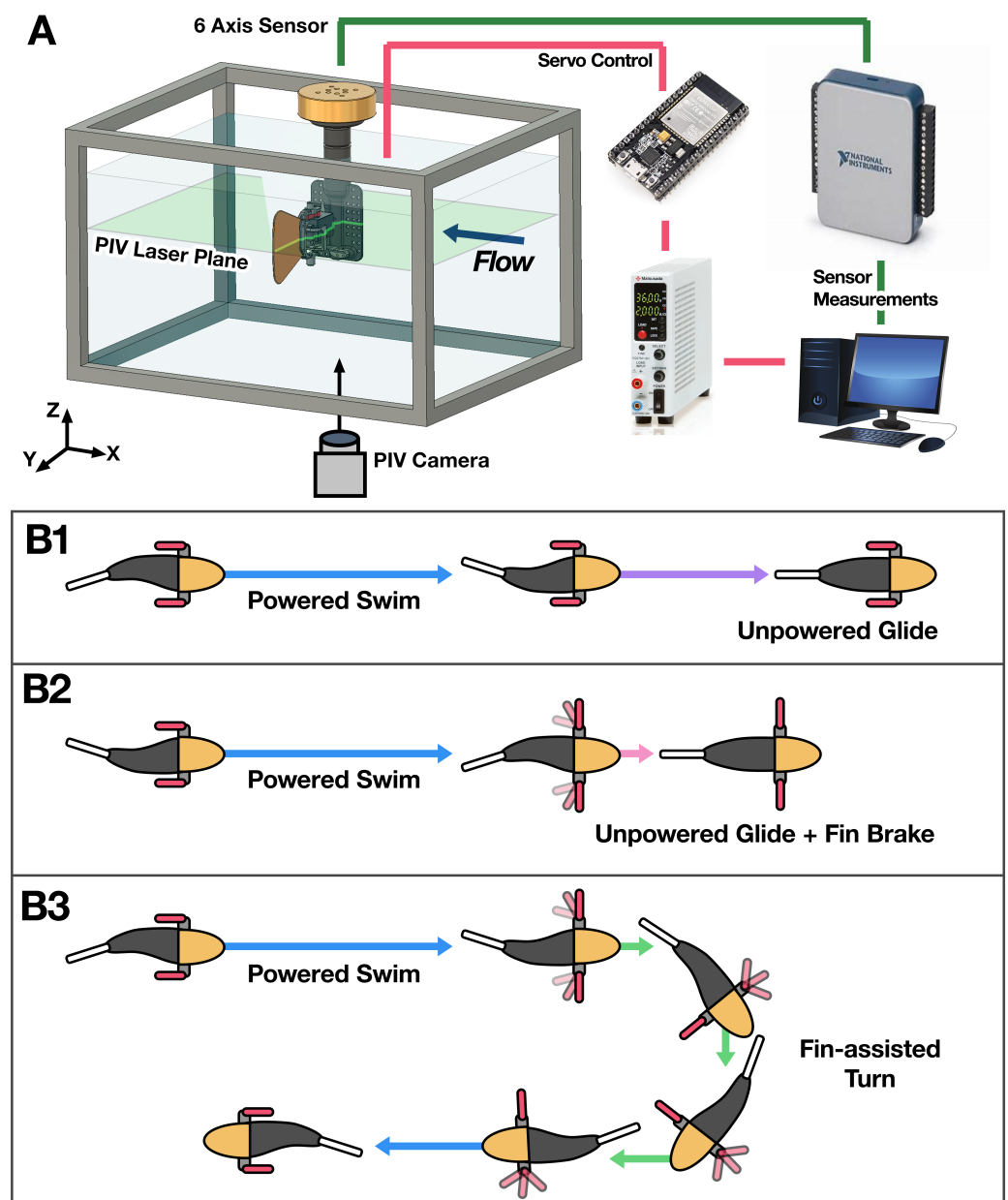

Figure 2. The experimental setup is designed to closely replicate the actual hardware configuration, utilizing a simplified hardware model. The system (**A**) includes a water circulation tank for simulation

purposes. underwater movement, a simplified pectoral fin mechanism, a microcontroller, a power supply, a six-axis force sensor, and a computer. The computer transmits commands to the microcontroller and collects force data from the sensor for analysis. A particle image velocimetry (PIV) system consisting of a continuous laser sheet and a high-speed camera is used for analysis of the flow characteristics. The laser plane is normal to the servo motor's actuation axis, and PIV camera is placed directly underneath the fin mechanism (Multimedia available online, Videos S1 and S2, Document S1). Panels (**B1**–**B3**) illustrate the three proposed swimming modes enabled by the pectoral fin mechanism. In (**B1**), both fins are retracted to minimize drag during normal swimming and gliding. (**B2**) shows the 'fin-assisted brake' mode, in which the robotic fish quickly deploys its pectoral fins to generate braking forces. (**B3**) demonstrates asymmetric fin deployment, where one fin flaps to produce sideways thrust, significantly reducing the turning radius for enhanced maneuverability.

2.3. Static Behavior of the Pectoral Fin Under Constant Flow Conditions

This experiment, the first in a series designed to investigate the hydrodynamic performance of a pectoral fin mechanism, was conducted within a controlled water circulation tank. Two flow speeds, 0.15 m/s and 0.3 m/s, were used to analyze the influence of the angle of attack of the pectoral fin on the lift and drag forces generated by the fin mechanism.

The pectoral fin was actuated incrementally from 0° to 180°, in 5° steps, to capture its hydrodynamic response in each orientation. For each angle of the fin, the lift and drag forces were measured over a 30 s interval and subsequently averaged to ensure consistent data. The averaged lift and drag values for each angle setting are presented in Figure 3.

From the plotted data, a clear trend in drag force was observed. The drag force increased with the angle of the fin, reaching its maximum at 80°, after which it decreased as the angle increased further. The lift force displayed a more complex pattern: starting from 0 at 0°, it decreased to a minimum at 35°, then increased, crossing 0 at 80° and continuing to rise, peaking around 135° before it began to decline again. These observed trends provide an initial understanding of the performance of the fin mechanism and lay the groundwork for a more detailed analysis in subsequent experiments.
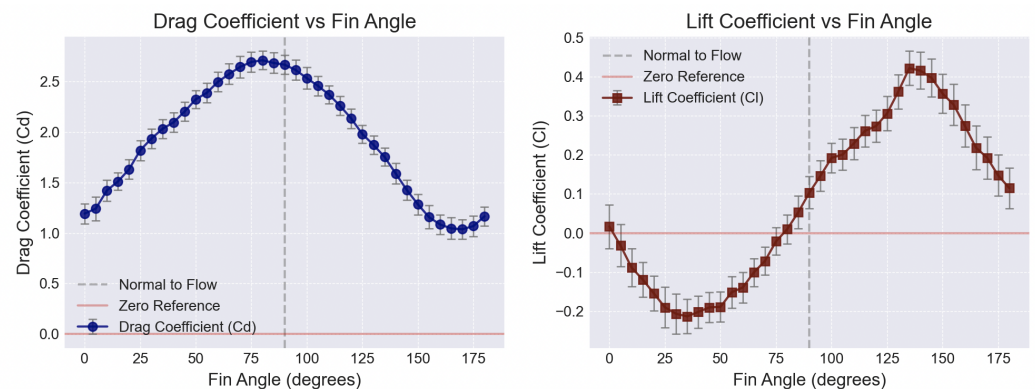

Figure 3. Lift and drag coefficients measured at 0.3 m/s, plotted against the fin attack angle with error bars.

2.4. Thrust Generation by the Pectoral Fin

To quantify the propulsive capabilities of our 1-DOF pectoral fin, we measured the time-averaged thrust and the RMS of the force normal to the thrust direction as functions of oscillation amplitude and frequency. Figure 4 presents these measurements as two-dimensional heat maps over the parameter space: (a) average combined force (thrust), and (b) RMS normal force (side–side stability).

At low amplitudes (<20°) and frequencies (<0.5 Hz), thrust production is minimal (<1 N), reflecting the small swept area and slow fluid acceleration. Thrust increases

monotonically with both amplitude and frequency, reaching a maximum of approximately 7.2 N near 65° amplitude and 1.75 Hz frequency (Figure 4a). This region represents the optimal trade-off between swept volume per stroke and the hydrodynamic response time of the fin.
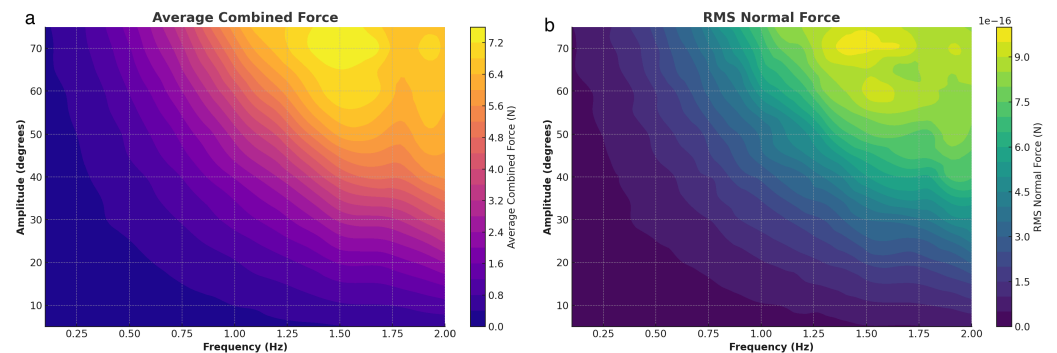

Figure 4. Average thrust (**a**) and force normal to thrust (RMS) (**b**), plotted against fin oscillation amplitude and frequency.

However, high amplitudes and frequencies also amplify force fluctuations transverse to the primary thrust axis, as shown by the RMS normal force map (Figure 4b). RMS values remain below 1×10^{-16} N at amplitudes below 30° and frequencies below 1 Hz, indicating smooth, predictable operation. Above 50° amplitude and 1.5 Hz frequency, RMS normal forces climb past 9×10^{-16} N, suggesting increased lateral loading and potential instability during fast strokes.

By overlaying these two metrics, we identify a sweet spot around 60° amplitude and 1.5 Hz frequency where thrust exceeds 6 N while RMS normal force remains below 6×10^{-16} N. We selected this operating point for all dynamic swimming tests, as it delivers high propulsive efficiency with acceptable stability.

2.5. Vortex Dynamics of Pectoral Fin Deceleration Under Constant Flow: Deceleration Rate Effects

Figure 5 presents the raw drag (X) and lift (Y) time-series measured during pectoral fin deployment to 80° in a steady 0.3 m/s flow. Each panel overlays three ramp durations—0.2 s (red), 1.0 s (blue), and 2.0 s (green), with solid lines showing the mean of three repeats and shaded bands indicating the data range. The 0.2 s ramp represents the fastest safe deceleration: beyond this, the servo stalls or skips steps, corrupting the commanded trajectory. The 2.0 s ramp is the slowest that avoids perceptible jitter (PWM switching noise appears at longer ramps due to low-speed torque ripple). The intermediate 1.0 s case provides a mid-point for parametric comparison. The lower insets plot the fin-angle command profiles for each ramp. The fastest deployment (0.2 s) produces a pronounced drag spike of ~12 N and a corresponding lift peak of ~4 N, followed by rapid decay and oscillations. Moderate (1.0 s) and slow (2.0 s) ramps yield progressively lower peak forces (~7 N and ~3 N, respectively) and longer transient responses, but with fewer high-frequency fluctuations.

To generalize these observations across a range of fin angles and ramp times, we defined four metrics from each X-force response: 1. t_1, the time from actuation onset to peak drag; 2. t_2, the interval from peak drag until drag settles within 3% of its quasi-steady value; 3. $t_1 + t_2$, the total stabilization time; and 4. The area under the drag curve over $t_1 + t_2$, representing the integrated transient impulse.
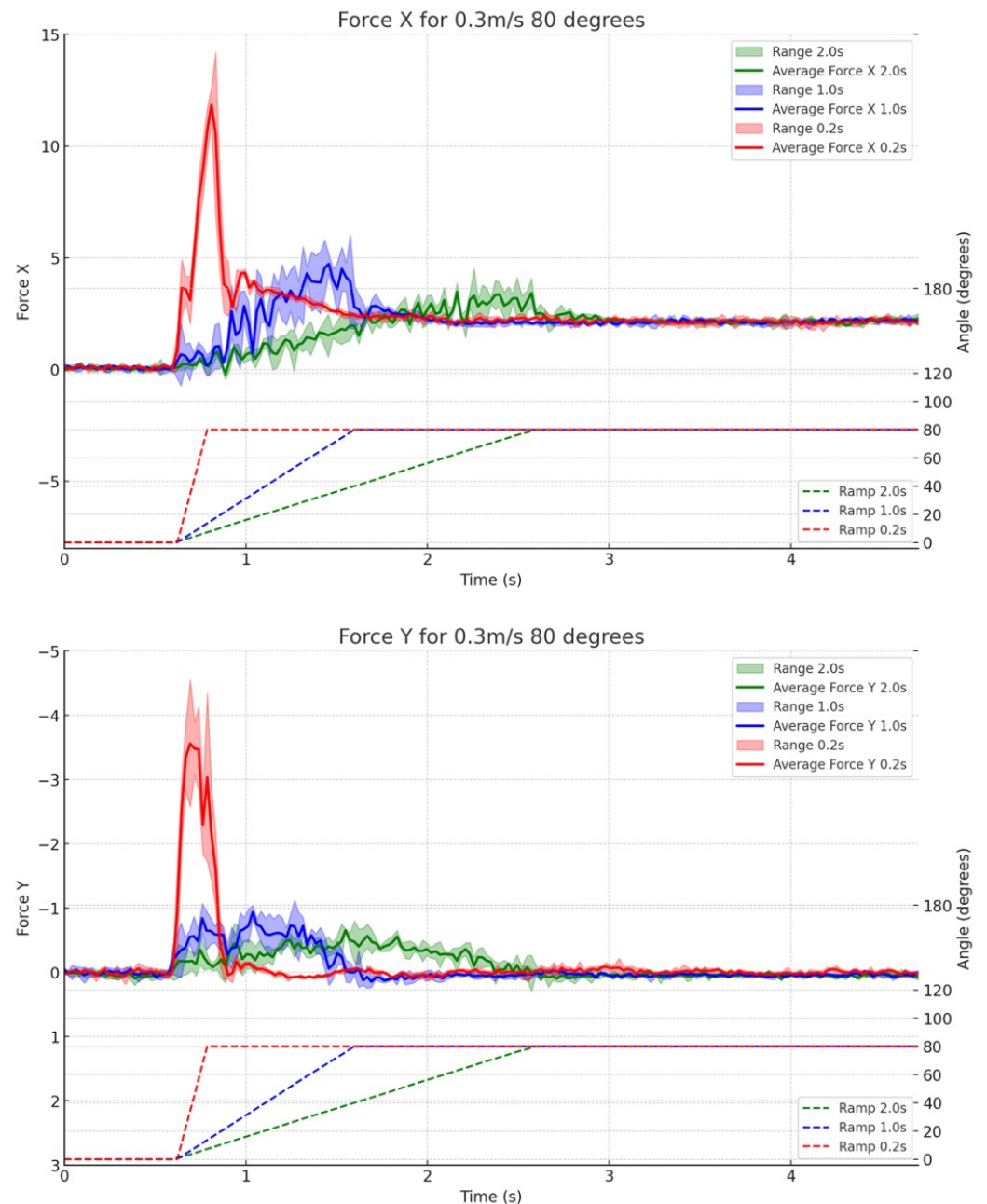
Figure 5. Drag and lift forces recorded during pectoral fin deployment, with the fin opening to 80 degrees in a steady 0.3 m/s flow. The fin's angle is controlled via a ramp signal, with ramp duration (in seconds) dictating the deployment speed to the final position. X and Y force data are measured and plotted over a 5 s interval. Each ramp time and angle combination is tested in triplicate for consistency.

Figure 6 shows contour maps of these four quantities plotted versus final fin angle (60–110°) and ramp duration (0.2–2.0 s). Short ramps minimize t_1 but amplify oscillatory tails (longer t_2), while slow ramps spread the force buildup (larger t_1) yet produce smoother responses (smaller t_2). The combined stabilization time $t_1 + t_2$ exhibits a clear minimum at intermediate ramp rates and mid-range angles, suggesting an optimal trade-off between responsiveness and stability. Likewise, the integrated impulse peaks in the rapid-ramp regime and drops off sharply for gentler deployments.
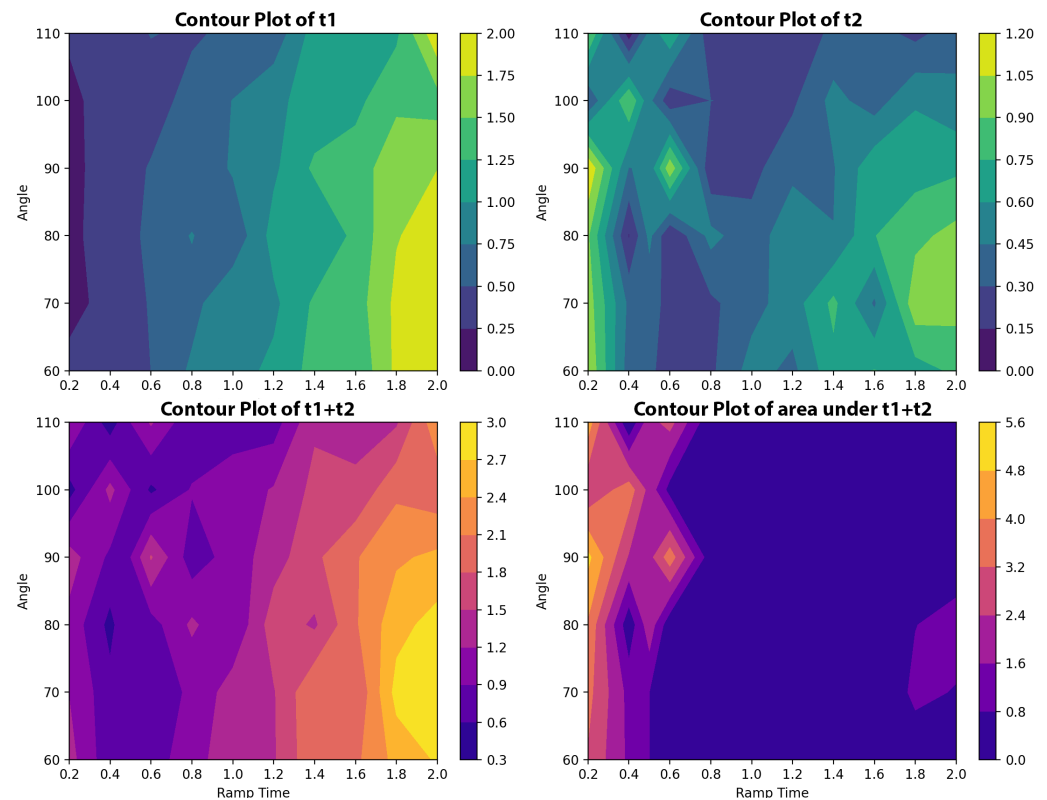
Figure 6. A composite plot with four subplots, each representing different metrics plotted against final fin angle and ramp duration. (**Top left**): t1—the time from initial fin actuation to peak drag. (**Top right**): t2—the time from peak drag until drag stabilizes within 3% of its final value. (**Bottom left**): t1 + t2, representing the total duration from actuation to stabilization. (**Bottom right**): the area under the curve for t1 + t2.

To resolve the transient flow structures during fin deceleration, time-resolved particle image velocimetry (TR-PIV) was synchronized with the robotic fish motion. The horizontal mid-span plane of the pectoral fin was illuminated by a 2 mm thick laser sheet, generated by a continuous 532 nm diode-pumped solid-state laser (SM-SEMI-532nm-10W (SM-SEMI, Shenzhen, China) 10 W output). Hollow glass spheres (Dantec Dynamics (Skovlunde, Denmark), density 1.1 g/cm³) were neutrally buoyant and seeded at 0.1 g/L to trace flow motions. A Photron(Tokyo, Japan) FASTCAM SA-Z camera (1280 × 1024 pixels) operated at 105 fps captured particle displacements, covering a 240 mm × 192 mm field of view around the fin trailing edge. Instantaneous velocity fields were computed using multi-pass cross-correlation (initial/final windows: 64 × 64 to 32 × 32 pixels, 50% overlap) with sub-pixel refinement via 2 × 3 Gaussian fitting, achieving a vector spacing of 3.75 mm. Phase-averaged vorticity fields were obtained by ensemble-averaging 50 motion cycles across 13 phase bins, ensuring statistical convergence of vortex dynamics.

2.5.1. Rapid Deceleration

The motion of the robotic fish in this study is characterized by its fin sweeping to an angle of 80° within 0.2 s, referred to as the Rapid Deceleration Group. This rapid kinematic transition induces significant changes in both the drag force and the dynamics of the surrounding fluid. By analyzing PIV snapshots at specific time intervals and correlating them with fluctuations in drag force, this section investigates vortex dynamics and their influence on drag force variation.

The drag force data (Figure 7) show a rapid increase during the initial phase ($t = 0$ to 0.5 s), reaching a peak at approximately 12 N. This sharp rise is due to the sudden generation of concentrated vortices at the trailing edge of the fin. At $t = 0.6$ s (Figure 7a),

the PIV snapshot reveals localized regions of intense vorticity and velocity gradients near the tail. These vortices are the result of the abrupt motion of the fin, creating a large pressure differential between the leading and trailing edges, which contributes to the peak drag force.

As the fin progresses into the transition phase ($t = 0.5$ to 2.0 s), the drag force decreases rapidly. At $t = 0.72$ s (Figure 7b), the vortices detach from the tail and advect downstream, elongating and dissipating in the wake. This reduces the pressure differential around the fin, causing a decrease in drag force. By $t = 0.8$ s (Figure 7c), the vortices become weaker and the drag force continues to decrease.

During the steady-state phase ($t > 2.0$ s), the drag force stabilizes at approximately 2 N. The PIV snapshots at $t = 1.0$ s (Figure 7d) and $t = 1.2$ s (Figure 7e) show weakened vortices in the wake, transitioning to a more turbulent flow regime. The drag force reaches a stable value around 2 N.
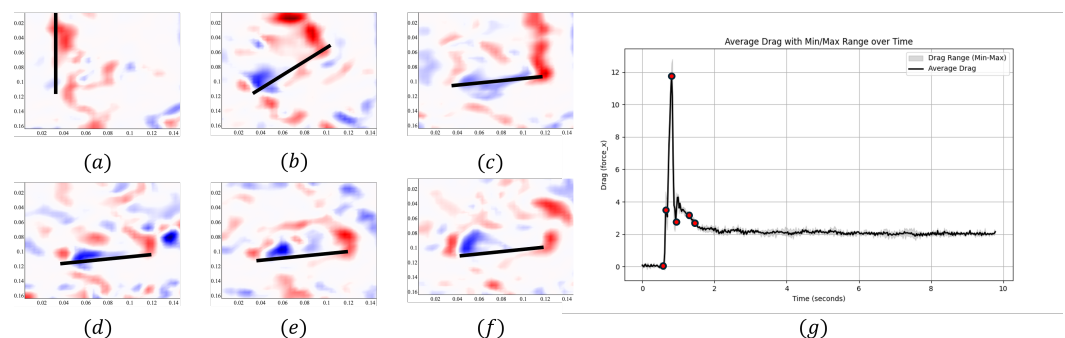

Figure 7. Snapshots (**a**–**f**) show vortex dynamics at the following time points: (**a**) $t = 0.6$ s, (**b**) $t = 0.72$ s, (**c**) $t = 0.8$ s, (**d**) $t = 1.0$ s, (**e**) $t = 1.2$ s, (**f**) $t = 1.36$ s. (**g**) the average drag force over time with corresponding minimum and maximum ranges. The red dots on plot (**g**) represent time points of (**a**–**f**) respectively.

2.5.2. Moderate Deceleration

The robotic fish's motion is characterized by its fin sweeping to an angle of 80° within 1 s, referred to as the Moderate Deceleration Group. This slower motion induces a more gradual change in drag force and surrounding flow field compared to the rapid deceleration group. By correlating PIV snapshots with drag force fluctuations, this section explores vortex dynamics and their influence on drag force variation.

The drag force data (Figure 8) show a moderate increase during the initial phase ($t = 0$ to 1.0 s), peaking at approximately 4.8 N. At $t = 0.6$ s (Figure 8a), the PIV snapshot reveals the initial formation of vortices near the trailing edge of the fin. The velocity gradients and vorticity intensity are lower than in the rapid deceleration group, resulting in a more gradual increase in drag force. By $t = 0.9$ s (Figure 8b), the vortices become larger and more coherent, leading to the observed drag force peak.

In the transition phase ($t = 1.0$ to 1.66 s), the drag force decreases as the vortices detach and advect downstream. At $t = 1.08$ s (Figure 8c), the PIV snapshot shows vortex detachment, with elongated structures in the wake, indicating a reduction in vortex intensity. By $t = 1.46$ s (Figure 8d), the vortices move downstream, dissipating energy into the surrounding fluid, causing a decline in drag force.

During the steady-state phase ($t > 1.66$ s), the drag force stabilizes at approximately 2.1 N. The PIV snapshots at $t = 1.66$ s (Figure 8e) and $t = 2.0$ s (Figure 8f) show regular and alternating vortex shedding patterns in the wake, indicating that the flow field has reached dynamic equilibrium.
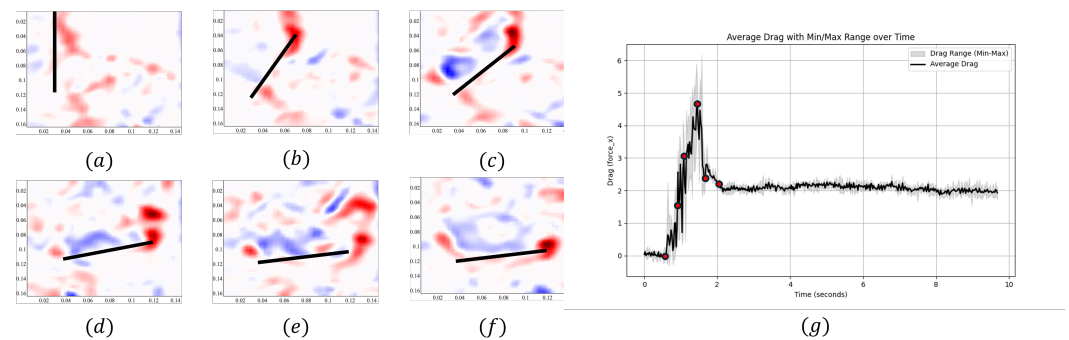
Figure 8. Snapshots (**a**–**f**) show vortex dynamics at the following time points: (**a**) $t = 0.6$ s, (**b**) $t = 0.9$ s, (**c**) $t = 1.08$ s, (**d**) $t = 1.46$ s, (**e**) $t = 1.66$ s, (**f**) $t = 2.0$ s. (**g**) the average drag force over time with corresponding minimum and maximum ranges. The red dots on plot (**g**) represent time points of (**a**–**f**) respectively.

2.5.3. Slow Deceleration

The motion of the robotic fish in this study is characterized by its fin sweeping to an angle of 80° in 2 s, called the slow decline group. This slower motion induces more gradual changes in both the drag force and the surrounding flow field compared to the previous groups. By analyzing PIV snapshots and correlating them with drag force fluctuations, this section provides insights into the vortex dynamics and their influence on drag force.

The drag force data (Figure 9) show a gradual increase during the initial phase ($t = 0$ to 2.0 s), reaching a peak at approximately 3.5 N. At $t = 0.6$ s (Figure 9a), the PIV snapshot shows the early formation of vortices near the trailing edge of the fin. Due to the slower motion, the velocity gradients and vorticity intensity are significantly lower compared to the moderate and rapid deceleration groups. By $t = 1.12$ s (Figure 9b), the vortices are larger but remain less intense, resulting in a smoother increase in drag force.

In the transition phase ($t = 2.0$ to 2.4 s), the drag force plateaus and decreases slightly as the vortices detach and advect downstream. At $t = 1.6$ s (Figure 9c), the PIV snapshot shows the gradual detachment of vortices with elongated structures in the wake, resulting in minimal fluctuations in drag force. By $t = 1.86$ s (Figure 9d), the detached vortices dissipate energy into the surrounding fluid and the drag force stabilizes.

During the steady-state phase ($t > 2.4$ s), the drag force stabilizes at approximately 2.1 N. The PIV snapshots at $t = 2.4$ s (Figure 9e) and $t = 2.8$ s (Figure 9f) show well-organized and periodic vortex shedding patterns, indicating that the flow has reached dynamic equilibrium. The stabilization of the drag force reflects the reduced intensity and smoother vortex detachment compared to faster fin movements.
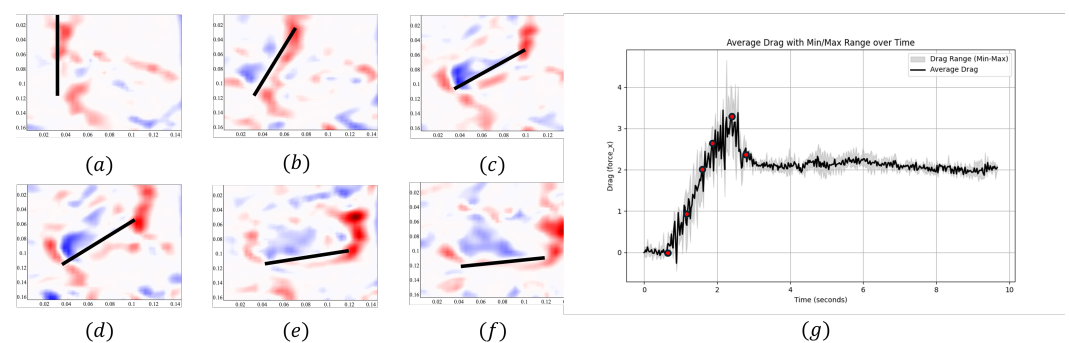

Figure 9. Snapshots (**a**–**f**) show vortex dynamics at the following time points: (**a**) $t = 0.6$ s, (**b**) $t = 1.12$ s, (**c**) $t = 1.6$ s, (**d**) $t = 1.86$ s, (**e**) $t = 2.4$ s, and (**f**) $t = 2.8$ s. (**g**) the average drag force over time with corresponding minimum and maximum ranges. The red dots on plot (**g**) represent time points of (**a**–**f**) respectively.

2.5.4. Comprehensive Comparison of Deceleration Groups

The three deceleration groups differ in vortex shedding mechanisms, wake dynamics, and drag force characteristics. Rapid deceleration generates compact, high-energy vortices that detach abruptly, creating turbulence and chaotic wake structures. Moderate deceleration produces smoother vortex formation and detachment, resulting in a more stable wake. Slow deceleration minimizes turbulence, creating a highly periodic and organized wake with reduced drag fluctuations.

The effects of braking time on the flow field are clear: shorter braking times amplify vortex intensity and cause abrupt force variations, while longer braking times lead to smoother interactions. This highlights the importance of deceleration timing in the hydrodynamic control of robotic fish propulsion.

2.5.5. Impact of Deceleration Time on Vortex Dynamics and Force Variation

Deceleration time significantly influences the interaction between the robotic fin and the surrounding fluid. Variations in vortex shedding intensity, detachment rate, and downstream wake patterns correspond directly to the braking time, creating distinct hydrodynamic characteristics across the deceleration groups.

Vortex Intensity and Detachment Rate

For the Rapid Deceleration Group, the short deceleration time of 0.2 s leads to intense vortex detachment. At $t = 0.6$ s (Figure 7a), the PIV snapshot shows tightly packed high-vorticity regions near the trailing edge. These vortices detach almost instantly, creating strong turbulence in the wake. Rapid detachment results in large fluctuations in drag force, with a peak of 12 N, reflecting the inability of the fluid to adapt quickly to sudden motion of the fin.

In contrast, the Moderate Deceleration Group exhibits smoother vortex detachment due to the 1.0-s deceleration time. At $t = 0.9$ s (Figure 8a), the vortices grow steadily before detaching. The delayed detachment allows for a more uniform pressure distribution around the fin, leading to a lower maximum drag force of 5 N. The wake transitions from turbulence to periodic vortex patterns as detachment slows.

For the Slow Deceleration Group, the longer braking time of 2.0 s minimizes vortex intensity and promotes controlled detachment. At $t = 1.6$ s (Figure 9c), the PIV snapshot shows weak and diffuse vortices near the trailing edge. Gradual detachment ensures steady energy transfer from the fin to the fluid, with minimal turbulence. The drag force stabilizes at 2.1 N, reflecting the organized wake observed at $t = 2.8$ s (Figure 9f).

Downstream Wake Patterns

The downstream wake evolution also differs across the deceleration groups. For the Rapid Deceleration Group, the wake is dominated by chaotic vortex patterns with significant energy dissipation. The lack of symmetry of the wake indicates an inefficient energy transfer from the fin to the fluid.

The Moderate Deceleration Group transitions to a more stable wake downstream. By $t = 1.46$ s (Figure 8d), the vortices exhibit periodic shedding, reducing turbulence. The wake becomes progressively more organized, reflecting the controlled energy transfer facilitated by the longer braking time.

The Slow Deceleration Group achieves the most symmetric and periodic wake patterns. At $t = 2.8$ s (Figure 9f), the wake is characterized by well-spaced vortices that propagate downstream with minimal disturbance. The stability of the wake and the efficiency of energy transfer highlight the advantages of prolonged deceleration in minimizing hydrodynamic losses.

2.5.6. Summary

The comparative analysis of the three deceleration groups highlights the critical role of braking time in influencing the hydrodynamic behavior of robotic fins. The key findings are summarized as follows.

- Rapid Deceleration (0.2 s): This condition induces intense and chaotic vortex shedding, resulting in high drag-force peaks and turbulent wake patterns. The sudden detachment of the fin causes significant energy dissipation and unsteady flow dynamics.
- Moderate Deceleration (1.0 s): Vortex formation and detachment are smoother, leading to reduced turbulence and more stable wake structures. The drag force peaks are lower and the wake evolves into periodic patterns downstream.
- Slow Deceleration (2.0 s): This condition minimizes vortex intensity and turbulence, leading to highly periodic and symmetric wake patterns. The drag force remains stable, indicating efficient energy transfer from the fin to the surrounding fluid.

3. Results

3.1. Deployment of Optimal Control Parameters of a Robotic Fish

The experimental results highlight a significant improvement in braking performance and maneuverability with the deployment of optimized control parameters for the pectoral fin. These findings suggest that our design offers substantial benefits, which we will now explore further in the discussion to understand the broader implications of these results for biomimetic robotic design. Experimental data revealed that the pectoral fins, when used as speed brakes, could generate substantial drag forces during rapid extension, resulting in enhanced deceleration. Specifically, the deployment of the pectoral fins reduced stopping times and distances by approximately 50% when compared to an unpowered glide, as shown in Figure 10 (top left). This improvement highlights the potential of the pectoral fin mechanism to achieve rapid and controlled braking in underwater environments.

The deceleration profiles further supported these findings. Robotic fish equipped with active pectoral fins exhibited a steeper deceleration curve than unpowered glide, indicating faster and more efficient braking dynamics. The ability to control the deployment dynamics of the fins, particularly the duration of the ramp during extension, allowed precise modulation of the drag forces. Faster deployment speeds produced higher drag forces, effectively mimicking the natural braking strategies of fish. These results emphasize the importance of control parameters in optimizing the braking performance of the fin mechanism.

3.2. Hydrodynamic Performance of the Pectoral Fin Mechanism

Our experimental analysis revealed distinct relationships between fin control parameters and hydrodynamic performance. Table 1 summarizes the key performance metrics across different experimental conditions.

Table 1. Summary of key performance metrics for the pectoral fin mechanism.

Parameter	Optimal Value	Performance Improvement
Fin angle for max drag	80°	1.68 N additional drag per fin
Fin angle for max lift	135°	0.42 N additional lift per fin
Parameters for max thrust	70° at 1.5 Hz	7.2 N of thrust per fin
Deploy time (braking)	0.2 s	50% less stopping distance

Static force measurements at 0.3 m/s flow velocity demonstrated that the maximum drag force occurred at a fin angle of 80°, as shown in Figure 3, while the maximum lift force was achieved at 135°.
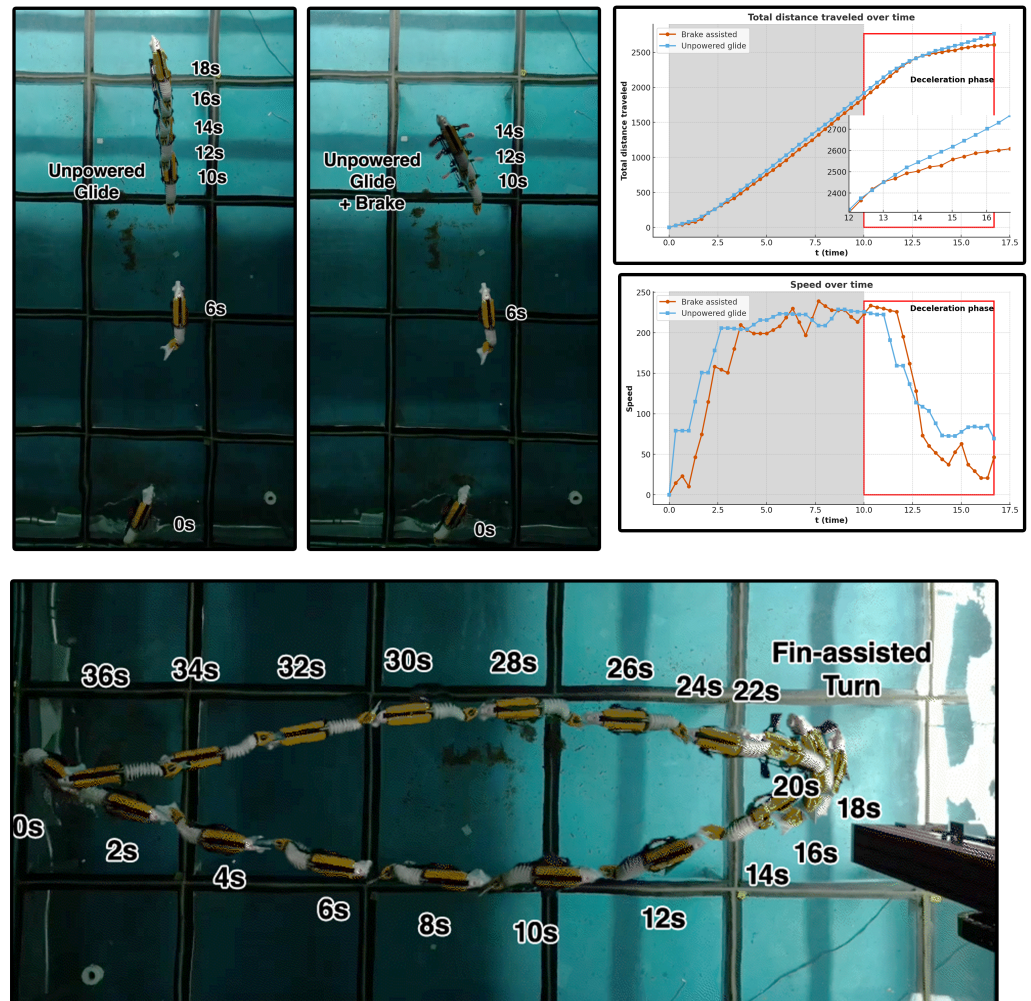
Figure 10. Free swimming performance comparisons: (**Top left**) images demonstrate substantial improvements in stopping performance when pectoral fins are deployed as speed brakes, reducing stopping time and distance by 50%. The (**top right**) plots compare deceleration profiles: pectoral fin brakes (right) achieve quicker deceleration than an unpowered glide (left). The (**bottom**) image illustrates a combined movement mode where fins are used for both propulsion and braking, enabling a "fin-assisted turn" that achieves a minimal turning radius (Multimedia available online, Videos S3–S5).

Dynamic testing revealed that rapid fin deployment (0.2 s ramp time) generated 12 N of peak drag force, higher than moderate deployment (1.0 s) which produced 5 N and slow deployment (2.0 s) which produced 2.1 N. The PIV analysis showed that slower deployment produced more organized wake patterns with less turbulent energy, suggesting a trade-off between immediate braking force and hydrodynamic efficiency.

When implemented on the SpineWave robot, the optimized fin parameters reduced stopping distance by 50% when compared to an unpowered glide at a swimming speed of 0.3 m/s.

3.3. Free Swimming Performance

The free swimming performance trials demonstrated the versatility of the pectoral fin mechanism to enable seamless integration of propulsion and braking functionalities. Our control architecture treats pectoral fins and the tail fin as separate subsystems, allowing independent mode transitions (e.g., retracted → braking → propulsion). For braking, the controller transitions the pectoral fins from 'glide' (0 °) to 'brake' (80 °) over the selected

deceleration ramp, while paused the tail undulation. These subsystems are run with each of their own time intervals to avoid interference. The robotic fish exhibited improved maneuverability through the use of pectoral fins for directional control, particularly in the execution of tight turning maneuvers. The "fin-assisted turn" mode, illustrated in Figure 10 (bottom), allowed the robotic fish to achieve minimal turning radii by leveraging the combined effects of lift and drag generated by the pectoral fins. This capability is critical for navigating complex underwater environments where precise and agile movements are required.

The experiments also highlighted the synergy between propulsion and braking during continuous swimming. By dynamically adjusting the position and motion of the fin, the robotic fish was able to smoothly transition between the propulsion and braking phases, maintaining both stability and efficiency. This dual functionality of the pectoral fins represents a significant advancement in the design of biomimetic underwater robots, as it eliminates the need for separate mechanisms for these functions. Furthermore, integration of the braking and propulsion mechanisms reduced overall energy expenditure, further improving the efficiency of the system.

In summary, optimized control of the pectoral fin mechanism not only enhanced the braking and maneuverability of the robotic fish but also demonstrated the effectiveness of biomimetic principles in addressing challenges in underwater robotics. These results provide a foundation for further exploration of biologically inspired designs in robotic systems.

4. Discussion

Incorporating a biomimetic pectoral fin system into the SpineWave robot has significantly improved its ability to stop and maneuver. This highlights the multifunctional nature of 1-DOF pectoral fins in enhancing both propulsion and control in underwater robots. The current design allows the pectoral fin to act as an effective speed brake, creating substantial drag that allows quick deceleration. This braking function mimics the natural tactics found in various fish species tailored for precise maneuvers in challenging aquatic settings [13,28]. Using the pectoral fin reduced the stopping time by nearly 50%, which is essential for applications that demand fast responses and precise control. The fin also boosts the robot's directional command, allowing it to perform sharper turns with smaller radii through the use of lift and drag forces, vital for navigating confined underwater environments like coral reefs and shipwrecks [29,30]. The straightforward actuation mechanism proves the viability of designs inspired by biology in marine robotics.

In our biomimetic robotic fish (equipped with two 1-DOF pectoral fins), the fin-based actuation offers several multifunctional advantages over traditional propellers. Each single-degree-of-freedom pectoral fin can serve as both a thrust generator and a control surface, enabling not only forward propulsion but also braking and lateral force for steering, much like the delta-shaped fins of rays that provide vectorial thrust and rudder-like control [31]. This means the robot can smoothly transition between propulsion modes (accelerating, stopping, turning) with minimal hardware complexity, since a single motor per fin suffices to produce forces in multiple directions. An added benefit of oscillating fin propulsion is the significantly lower acoustic noise signature; flapping fins operate more quietly and are harder to detect compared to small propellers [32,33]. Such stealthy operation is advantageous for underwater applications (e.g., environmental monitoring or covert inspection) where disturbance must be minimized. On the other hand, conventional propeller thrusters still tend to achieve higher propulsive efficiency during sustained straight-line cruising. Propellers are engineered for continuous rotation at a designed speed, which can make them more energy-efficient in steady forward motion and relatively

insensitive to small manufacturing variations in blade shape. In contrast, fin mechanisms can be more sensitive to precise fabrication and control tuning to reach their optimal efficiency. Overall, there is a trade-off between the two approaches: propellers excel in delivering efficient constant thrust for cruising, whereas biomimetic fins grant superior maneuverability, multi-axis control, and low-noise operation [34,35].

Despite significant advancements, the current system has limitations requiring resolution for maximum potential. These concerns are leading to future modifications, especially enhancing pectoral fin flexibility and adaptability. While the existing 1DOF model simplifies mechanics and conserves energy, it hinders 3D navigation. Fish naturally employ flexible pectoral fins for intricate maneuvers. Advanced models like four-bar linkages or 2DOF fins could offer the robot similar flexibility [36,37].

Another potential enhancement lies in the combined use of the pectoral fin and tail fin for propulsion. In this study, the pectoral fin was tested primarily as a braking and turning mechanism, while propulsion was driven by the tail fin. However, the simultaneous use of both fins could yield additional benefits [38,39]. For example, utilizing both fins during swimming can help reduce head motion, thus stabilizing any cameras or sensors onboard [40]. This stabilization would improve the robot's ability to capture clear visual data during exploration or monitoring missions. Furthermore, combined fin propulsion could potentially increase the robot's top speed, as median and/or paired fins(MPF) fish use body fins as the main means of propulsion [41–45]. Although this dual-fin propulsion mode may not be the most energy-efficient strategy, the trade-off between energy consumption and performance could be optimized based on specific mission requirements. Exploring this hybrid propulsion mode would require conducting experiments on a motion platform. This is beyond the scope of our current research, but we hope to explore it in the future.

Strengthening the mechanical durability and adaptability of the pectoral fin is vital. The existing rigid setup with fixed controls limits its responsiveness to varying flow conditions. Future designs might incorporate adaptive materials or variable stiffness to modulate the fin's shape and movements according to hydrodynamic forces [46–48]. We also plan to explore the possibility of embedding flex-sensors to the motion assembly. This would give the fish smart sensing capabilities and allow it to closely emulate the fluid dynamics of natural fish. The rigidity of the mechanical structure can also be improved to reduce flexing and give more consistent results. We plan to replace PLA with carbon fiber reinforced composites to greatly enhance rigidity without adding extra weight.

Investigating the fin's control strategy is also crucial. Currently, it relies on predefined motion sequences, which may not allow real-time adaptability. Introducing machine learning or feedback loops could enable the robot to adjust its fin movements based on sensor inputs [49–51]. This would allow for optimized braking based on water flow speed or improved turn angles to navigate obstacles more effectively, thereby enhancing underwater maneuverability and efficiency.

While the pectoral fin has improved the SpineWave robot's stopping and turning abilities, forthcoming advancements such as additional degrees of freedom, adaptive materials, and smart controls could further boost its agility, stability, and efficiency, rendering it more suitable for underwater exploration and surveillance.

5. Conclusions

The integration of the biomimetic pectoral fin mechanism into the SpineWave robot has substantially enhanced its braking and maneuverability, showcasing the power of biomimetic design in the advancement of underwater robotics. The fin's ability to execute rapid stops and sharp turns, while maintaining minimal mechanical complexity, underscores its practical effectiveness and potential for real-world applications.

Although the current single-degree-of-freedom (1-DOF) design has proven to be reliable, future iterations that incorporate combined propulsion modes and multi-degree-of-freedom (multi-DOF) fins hold the promise of further improving agility, speed, and stability. These advancements could unlock new capabilities for the SpineWave, broadening its potential in underwater exploration, inspection, and environmental monitoring, where precise control and adaptability are critical.

In summary, this study lays a strong foundation for future research and development in biomimetic robotic systems. It highlights how simple yet innovative designs, inspired by nature, can lead to substantial improvements in robotic performance. Building on these results, further developments are likely to push the limits of what is possible in underwater robotics, creating more efficient, versatile, and autonomous systems for a variety of marine applications.

Supplementary Materials: The following supporting information can be downloaded at: https://www.mdpi.com/article/10.3390/jmse13071295/s1, Video S1: FinPIV1. Video S2: FinPIV2. Video S3: AssistedTurn. Video S4: BrakeAssist. Video S5: UnpoweredGlide.. Document S1: PectoralFinSupplementaryPictures.

Author Contributions: Conceptualization, Q.H., Y.Z., and D.F.; methodology, Q.H., Y.Z., and D.F.; software, Q.H. and Y.Z.; validation, Q.H., Y.Z., and W.L.; formal analysis, Q.H. and Y.Z.; investigation, Q.H. and Y.Z.; resources, W.L., W.C., and D.F.; data curation, Q.H. and Y.Z.; writing—original draft preparation, Q.H. and Y.Z.; writing—review and editing, W.L., W.C., and D.F.; visualization, Q.H. and Y.Z.; supervision, W.L., W.C., and D.F.; project administration, W.C. and D.F.; funding acquisition, W.C. and D.F. All authors have read and agreed to the published version of the manuscript.

Data Availability Statement: The data presented in this study are available on request from the corresponding author.

Conflicts of Interest: The authors declare no conflicts of interest.

References

1. Wilga, C.D.; Lauder, G.V. Locomotion in sturgeon: Function of the pectoral fins. *J. Exp. Biol.* **1999**, *202*, 2413–2432. [CrossRef]
2. Liao, J.C. A review of fish swimming mechanics and behaviour in altered flows. *Philos. Trans. R. Soc. Biol. Sci.* **2007**, *362*, 1973–1993. [CrossRef]
3. Videler, J.J. *Fish Swimming*; Fish & Fisheries Series; Springer: Berlin/Heidelberg, Germany, 1993; pp. 1–121.
4. Green, A.L.; Maypa, A.P.; Almany, G.R.; Rhodes, K.L.; Weeks, R.; Abesamis, R.A.; Gleason, M.G.; Mumby, P.J.; White, A.T. Larval dispersal and movement patterns of coral reef fishes, and implications for marine reserve network design. *Biol. Rev.* **2015**, *90*, 1215–1247. [CrossRef] [PubMed]
5. Coates, M.I. The evolution of paired fins. *Theory Biosci.* **2003**, *122*, 266–287. [CrossRef]
6. Diogo, R.; Chardon, M. On the comparative anatomy of the Teleostei pectoral and pelvic girdles and associated muscles. *Cybium* **2007**, *25*, 337–349. [CrossRef]
7. Thorsen, D.H.; Westneat, M.W. Diversity of pectoral fin structure and function in fishes with labriform propulsion. *J. Morphol.* **2005**, *263*, 1155–1167. [CrossRef] [PubMed]
8. Kato, N. Control performance in the horizontal plane of a fish robot with mechanical pectoral fins. *IEEE J. Ocean. Eng.* **2000**, *25*, 121–129. [CrossRef]
9. Sitorus, P.; Nazaruddin, Y.; Leksono, E.; Budiyono, A. Design and implementation of paired pectoral fins locomotion of labriform fish applied to a fish robot. *J. Bionic Eng.* **2009**, *6*, 37–45. [CrossRef]
10. Tangorra, J.L.; Lauder, G.V.; Hunter, I.W.; Mittal, R.; Madden, P.G.; Bozkurttas, M. The effect of fin ray flexural rigidity on the propulsive forces generated by a biorobotic fish pectoral fin. *J. Exp. Biol.* **2010**, *213*, 4043–4054. [CrossRef]

11. Dong, H.; Bozkurttas, M.; Mittal, R.; Madden, P.; Lauder, G.V. Computational modeling and analysis of the hydrodynamics of a highly deformable fish pectoral fin. *J. Fluid Mech.* **2010**, *645*, 281–312. [CrossRef]

12. Lauder, G.V.; Madden, P.G. Morphology and experimental hydrodynamics of fish fin control surfaces. *IEEE J. Ocean. Eng.* **2004**, *29*, 556–571. [CrossRef]

13. Westneat, M.W.; Lenon, W.; Wainwright, P.C.; Ashley-Ross, M. Structure, function, and evolution of seahorse tailgrasping appendages. *Proc. R. Soc. Lond. Biol. Sci.* **2004**, *29*, 11–17. [CrossRef]

14. Hove, J.; O'Bryan, L.; Gordon, M.; Webb, P.; Weihs, D. Boxfishes (Teleostei: Ostraciidae) as a model system for fishes swimming with many fins: Kinematics. *J. Exp. Biol.* **2001**, *204*, 1459–1471. [CrossRef] [PubMed]

15. Gibb, A.; Jayne, B.; Lauder, G. Kinematics of pectoral fin locomotion in the bluegill sunfish Lepomis macrochirus. *J. Exp. Biol.* **1994**, *189*, 379–387. [CrossRef]

16. Chu, W.S.; Lee, K.; Song, S.H.; Han, M.W.; Lee, J.Y.; Kim, H.S.; Kim, M.S.; Park, Y.J.; Cho, K.J.; Ahn, S.H. A review of biomimetic underwater robots using smart materials. *Smart Mater. Struct.* **2012**, *13* , 053001.

17. Lauder, G.V.; Anderson, E.J.; Tangorra, J.; Madden, P.G. Fish biorobotics: Kinematics and hydrodynamics of self-propulsion. *J. Exp. Biol.* **2007**, *210*, 2767–2780. [CrossRef]

18. Raj, A.; Thakur, A. Fish-inspired robots: Design, sensing, actuation, and autonomy—A review of research. *Bioinspir. Biomim.* **2016**, *11*, 031001. [CrossRef]

19. Ryuh, Y.; Yang, G.; Liu, J.; Hu, H. School of swimming robots: Modeling, design, and motion coordination. *J. Mech. Sci. Technol.* **2015**, *12*, 4265–4273. [CrossRef]

20. Shin, D.; Tanaka, N.; Kim, H.; Kang, B.; McIntosh, J. Fish robotics: Biomimetic approaches for aquatic propulsion. *Mar. Technol. Soc. J.* **2007**, *1*, 4–17. [CrossRef]

21. Tokekar, P.; Branson, E.; Vander Hook, J.; Isler, V. Tracking aquatic invaders: Autonomous robots for monitoring invasive fish. *IEEE Robot. Autom. Mag.* **2013**, *20*, 33–41. [CrossRef]

22. Xie, H.; Shen, J.; Fan, Y.; Pan, X.; Ni, Z.; Jiao, Y. Designs of the biomimetic robotic fishes performing Body and/or Caudal Fin (BCF) swimming locomotion: A review. *Appl. Sci.* **2021**, *102*, 1–22. [CrossRef]

23. Yuh, J.; Marani, G.; Blidberg, D.R. Underwater robotics. *Annu. Rev. Control. Robot. Auton. Syst.* **2001**, *15*, 245–268. [CrossRef]

24. Sivčev, S.; Coleman, J.; Omerdić, E.; Dooly, G.; Toal, D. Underwater manipulators: A review. *Ocean. Eng.* **2018**, *163*, 433–450. [CrossRef]

25. Barbera, G.; Currò, D.; Sutera, A. Attitude control for a pectoral fin actuated bio-inspired robotic fish. *Control Eng. Pract.* **2011**, 809–818. [CrossRef]

26. Behbahani, S.B.; Tan, X. Bio-inspired flexible joints with passive feathering for robotic fish pectoral fins *Bioinspir. Biomim.* **2016**, *11*, 036009. [CrossRef]

27. Higham, T.E.; Malas, B.; Jayne, B.C.; Lauder, G.V. Constraints on starting and stopping: Behavior compensates for reduced pectoral fin area during braking of the bluegill sunfish Lepomis macrochirus. *J. Exp. Biol.* **2005**, *208*, 4735–4746. [CrossRef]

28. Gerstner, C.L. Maneuverability of four species of coral-reef fish that differ in body and pectoral-fin morphology. *Can. J. Zool.* **1999**, *77*, 1102–1110. [CrossRef]

29. Luong, J.; Glick, P.; Arias, A.; Nagpal, R.; Morin, S. Eversion and retraction of a soft robot towards the exploration of coral reefs. *Adv. Robot.* **2019**, 1122–1134. [CrossRef]

30. Bingham, B.; Foley, B.; Singh, H.; Camilli, R.; Delaporta, K.; Eustice, R.; Mallios, A.; Mindell, D.; Roman, C.; Sakellariou, D. Robotic tools for deep water archaeology: Surveying an ancient shipwreck with an autonomous underwater vehicle. *J. Field Robot.* **2010**, *27*, 223–237. [CrossRef]

31. Chen, L.; Bi, S.; Cai, Y.; Cao, Y.; Pan, G. Design and experimental research on a bionic robot fish with tri-dimensional soft pectoral fins inspired by cownose ray. *J. Mar. Sci. Eng.* **2022**, *10*, 537. [CrossRef]

32. Szymak, P.; Piskur, P.; Kot, R.; Naus, K.; Powarzyński, D. Biomimetic propulsion system efficiency for unmanned underwater vehicle. *Sci. Rep.* **2025**, *15*, 11086. [CrossRef]

33. Marino, L. Experimental analysis of UAV propeller noise. In Proceedings of the 16th AIAA/CEAS Aeroacoustics Conference, Stockholm, Sweden, 7–9 June 2010; p. 3854.

34. Maertens, A.; Triantafyllou, M.S.; Yue, D.K. Efficiency of fish propulsion. *Bioinspir. Biomim.* **2015**, *10*, 046013. [CrossRef] [PubMed]

35. Fish, F.E. Advantages of natural propulsive systems. *Mar. Technol. Soc. J.* **2013**, *47*, 37–44. [CrossRef]

36. Zhong, Y.; Yang, W.; Wang, X.; Song, J.; Guo, Y.; Du, J. Design and experimental results of a compliant oscillation propulsion mechanism on a self-propelling robotic fish. *Appl. Phys. A* **2013**, *78*, 879–885.

37. Palmisano, J.S.; Geder, J.D.; Ramamurti, R.; Sandberg, W.C.; Ratna, B. Robotic pectoral fin thrust vectoring using weighted gait combinations. *Appl. Bionics Biomech.* **2012**, *9*, 501–512. [CrossRef]

38. Hale, M.E.; Day, R.D.; Thorsen, D.H.; Westneat, M.W. Pectoral fin coordination and gait transitions in steadily swimming juvenile reef fishes. *J. Exp. Biol.* **2006**, *209*, 3708–3718. [CrossRef]

39. Fish, F.E.; Shannahan, L.D. The role of the pectoral fins in body trim of sharks. *J. Fish Biol.* **2000**, *56*, 1062–1073. [CrossRef]

40. Qiu, H.; Chen, L.; Ma, X.; Bi, S.; Wang, B.; Li, T. Analysis of Heading Stability due to Interactions between Pectoral and Caudal Fins in Robotic Boxfish Locomotion. *J. Bionic Eng.* **2023**, *20*, 390–405. [CrossRef]

41. Harris, J.E. The role of the fins in the equilibrium of the swimming fish: II. The role of the pelvic fins. *J. Exp. Biol.* **1938**, *15*, 32–47. [CrossRef]

42. Blevins, E.L.; Lauder, G.V. Rajiform locomotion: Three-dimensional kinematics of the pectoral fin surface during swimming in the freshwater stingray Potamotrygon orbignyi. *J. Exp. Biol.* **2012**, *215*, 3231–3241. [CrossRef]

43. Blake, R.W. Fish functional design and swimming performance. *J. Fish Biol.* **2004**, *65*, 1193–1222. [CrossRef]

44. Sfakiotakis, M.; Lane, D.M.; Davies, J.B.C. Review of fish swimming modes for aquatic locomotion. *IEEE J. Ocean. Eng.* **1999**, *24*, 237–252. [CrossRef]

45. Webb, P.W. The biology of fish swimming. *Mech. Physiol. Anim. Swim.* **1994**, 45–62. [CrossRef]

46. Yen, W.K.; Sierra, D.M.; Guo, J. Controlling a robotic fish to swim along a wall using hydrodynamic pressure feedback. *IEEE J. Ocean. Eng.* **2018**, *43*, 369–380. [CrossRef]

47. Liu, G.; Wang, A.; Wang, X.; Liu, P. A Review of Artificial Lateral Line in Sensor Fabrication and Bionic Applications for Robot Fish. *Appl. Bionics Biomech.* **2016**, *2016*, 4732703. [CrossRef]

48. Zheng, X.; Wang, C.; Fan, R.; Xie, G. Artificial lateral line based local sensing between two adjacent robotic fish. *Bioinspir. Biomim.* **2017**, *13*, 016002. [CrossRef]

49. Sun, B.; Li, W.; Wang, Z.; Zhu, Y.; He, Q.; Guan, X.; Dai, G.; Yuan, D.; Li, A.; Cui, W. Recent progress in modeling and control of bio-inspired fish robots. *J. Mar. Sci. Eng.* **2022**, *10*, 773. [CrossRef]

50. Ren, Q.; Xu, J.; Li, X. A data-driven motion control approach for a robotic fish. *J. Bionic Eng.* **2015**, *12*, 382–394. [CrossRef]

51. Liu, J.; Hu, H.; Gu, D. A hybrid control architecture for autonomous robotic fish. In Proceedings of the 2006 IEEE/RSJ International Conference on Intelligent Robots and Systems, Beijing, China, 9–15 October 2006; IEEE: Piscataway, NJ, USA, 2006; pp. 312–317.